On the modeling of a visco-hyperelastic polymer gel under blunt ballistic impacts

Anthony Bracq, Grégory Haugou, Benjamin Bourel, Christophe Maréchal, Franck Lauro, Sébastien Roth, Olivier Mauzac

International Journal of Impact Engineering 118 (2018) 78–90

On the modeling of a visco-hyperelastic polymer gel under blunt ballistic impacts

A. Bracq[a,*], G. Haugou[a], B. Bourel[a], C. Maréchal[a], F. Lauro[a], S. Roth[b], O. Mauzac[c]

[a] Laboratory LAMIH UMR CNRS 8201, University of Valenciennes, Valenciennes 59313, France
[b] University of Bourgogne Franche-Comté, UTBM, Interdisciplinary Carnot laboratory of Bourgogne UMR CNRS 6303, Belfort 90010, France
[c] French Ministry of the Interior, CREL/SAELSI, Place Beauveau, Paris, France

ABSTRACT

In this paper, the modeling of a polymer gel used as target medium in blunt ballistic experiments is presented. A new visco-hyperelastic law based on the Mooney–Rivlin model is proposed and implemented in a numerical simulation software. The material model identification relies on mechanical characterization experiments per-formed at room temperature through tensile and compressive tests over a wide range of strain rates (0.002–1500 s^{-1}). Indeed, these experiments highlight a significant strain rate sensitivity but also a non-homogeneous strain and a barreling effect during compressive experiments. Hence, constitutive modeling of the material behavior cannot be directly determined. Tensile and compressive data are exploited with a direct and indirect identification process. An optimization by inverse technique, using finite element modeling of static and dynamic compressive tests and a global response surface method, is employed to accurately reproduce loading conditions and identify the model parameters. Finally, the proposed visco-hyperelastic law is validated through comparison with experimental data from blunt ballistic impacts over various projectile velocities.

Keywords: Blunt ballistic impact; Soft material; Mechanical characterization; Constitutive modeling; Impact modeling

1. Introduction

Over the past few decades, there has been an increasing interest in ballistic blunt trauma. Trauma may be caused by the armor deformation and are so called Behind Armor Blunt Trauma (BABT). Moreover, impacts of Less-Lethal Kinetic Energy projectiles (LLKE) used by law enforcement officers may also lead to serious physiologic and physical injuries. A lot of researchers have reported cases describing injury patterns related to the impact of LLKE projectiles [1–5]. Becoming a public health concern, investigations have emerged on the use of Post-Mortem Human Subjects (PMHS) and anesthetized animals in order to gain insight into ballistic blunt trauma [6–8]. As the human torso is the major site of impacts in ballistic cases, researchers have focused their studies on this location. Despite the numerous benefits of these surrogates, practical and ethical issues have led scientists to elaborate and use homogeneous materials as human body substitutes.

The two conventional soft materials employed in this research field are 10 and 20 wt% ballistic gelatin. Even if these materials are generally used to understand human soft tissues behavior during penetrating ballistic events [9,10], studies have made use of ballistic gelatin to assess behind armor deformation [11–14]. Nevertheless, many studies have highlighted the numerous drawbacks of the ballistic gelatin, such as a precipitate aging time and an important temperature sensitivity, which complicate the experimental set-up [15,16]. Among various soft materials employed as ballistic testing medium, the synthetic polymer SEBS gel (styrene-ethylene-butylene-styrene) has numerous benefits, such as its environmental stability, transparency and mechanical consistency [17,18].

Consequently, these benefits have led the research center of the French Ministry of the Interior to use the SEBS gel as target medium for blunt ballistic impacts interpretation. Despite the measurement of the dynamic gel wall deformation, it is insufficient to completely assess blunt trauma. Therefore, numerical tools such as Finite Element (FE) method and smoothed particle hydrodynamics have been employed in recent studies to obtain extensive information during ballistic events [19–21]. However, a consistent constitutive material modeling is needed to accurately predict the impact phenomenon with mechanical characterization experiments.

Bracq et al. [22] have carried out such experiments on the SEBS gel material used in the current study over a wide range of strain rates. Tensile tests were performed using an appropriate gripping device and local strain measurement technique. As compression is the primary loading mode during impact, compressive tests were performed using a servo-hydraulic testing machine for quasi-static and intermediate strain

* Corresponding author.
E-mail address: Anthony.Bracq@univ-valenciennes.fr (A. Bracq).

DOI : 10.1016/j.ijimpeng.2018.04.001

rates. To capture the material behavior at higher strain rates, the authors used the well-known Split-Hopkinson Pressure Bars (SHPB) apparatus developed by Kolsky [23]. More precisely, polymeric bars have been used to obtain a significant signal to noise ratio due to the low impedance of the SEBS gel. Indeed, previous studies mentioned the use of such bars to determine the dynamic behavior of soft materials [24–27]. Bracq et al. [22] have highlighted a hyperelastic behavior with a hardening effect when strain rate increases. The use of high-speed imaging during compression experiments has shown the presence of a barreling effect and a non-homogeneous radial strain propagating through the sample. Hence, complete material behavior cannot be directly identified through mechanical testing.

Progress in numerical tools and optimization algorithms enables researchers to employ an inverse technique to determine the precise material response of materials exploiting experimental datasets [28,29]. Fontenier et al. [30] used this method based upon the modeling of indentation tests to calibrate material model parameters of a polymer gel brain substitute. Barreling effect by considering the friction between plates and specimen during compression events can be considered with FE modeling [31]. The study of Oliveira et al. [32] is an example of the accurate modeling of SHPB experiments to identify material model parameters. Experimental results or strain gauge signals over time have been used in the objective function to determine the related parameters.

However, a convenient constitutive law has to be chosen or developed in order to both simplify the identification procedure and obtain a reliable FE model. Over the last decade, very soft materials, as for instance elastomeric gels and ballistic gelatin, have been modeled by diverse constitutive laws. A literature review indicates an increasing complexity of constitutive laws taking into account the large strain and non-linear behavior, the strain rate dependence or the hydrodynamic behavior for very high speed impacts. The large strain ability or the hyperelasticity of the Sylgard gel has been mainly modeled using the well-known Mooney–Rivlin material model [30,33]. To model material behavior at even higher strains, the general Ogden material model has also been employed to predict the behavior of ballistic gelatin subjected to ballistic events [34]. Such complex materials often show a particular strain rate sensitivity. The generalized Maxwell model using Prony series has been adopted to consider the viscoelastic part of ballistic gelatin and incompressible rubber for a specific range of strain rates [34–36]. More precisely, Yang et al. [36] indicate that a sufficient number of relaxation times is required to cover static to dynamic strain rates. This conclusion was also supported by Cronin [34] which highly complicates the identification of model parameters. Therefore, researchers have used tabulated hyperelastic data from compression experiments to cover the material behavior across the range of strain rates considered [21,34,37]. This method has proved its ability to give both consistent results and simplify the modeling of visco-hyperelastic materials. However, to the authors' knowledge, no previous study has investigated the modeling of the SEBS gel material. It exhibits a hyperelastic behavior with a specific strain rate dependence over a wide range of strain rates. Thus, the viscoelastic model using Prony series added to the hyperelastic feature is not convenient for this study. Moreover, to exploit tensile and compressive tests whether or not experimental data are directly expendable, the use of tabulated hyperelastic data is not appropriate for this work.

Consequently, the aim of the present study is to propose a novel and suitable visco-hyperelastic constitutive law to model the gel SEBS behavior subjected to non-penetrating ballistic events. Firstly, the material used in the current study and its preparation are briefly described. Then the mechanical experiments of Bracq et al. [22] are succintly summarized. Secondly, the constitutive material model developed in this work is presented. Thirdly, the identification procedure based upon experiments, FE modeling and optimization algorithms is depicted. Finally, the robustness of the material model is highlighted through comparisons of ballistic experiments with respective FE modeling at diverse projectile velocities.

2. Material and sample preparation

The material used in this work is the SEBS (styrene-ethylene-butylene-styrene) tri-block copolymers provided by Kraton Polymers LLC (Kraton G1652). A SEBS gel is constituted by mixing SEBS powder and mineral oil with 30 wt% of SEBS having a styrene/elastomer ratio of about 30/70%. The white mineral oil is a PRIMOL 352 provided by ESSO S.A.L. The material density is about 880 kg/m^3. The mineral oil is preheated for 2 h at 100 °C in a metallic drum placed in an oven. The SEBS powder is gradually added while mixing continuously. The mixture temperature is increased to 150 °C and soaked for 4 h with regular mixing. Once completely melted and free of bubbles, the liquid is poured into a dedicated mold to produce test samples for mechanical testing or gel blocks for ballistic testing.

3. Experimental results

First of all, the tensile response at very high strain of the SEBS gel has been examined over various strain rates. The highly compliant nature of the material has forced Bracq et al. [22] to adopt specific tensile aluminum grips and dedicated local strain measurements. The analysis of transverse and longitudinal elongations ensure the assumption of material incompressibility. Both load data and strain measurements lead to the true stress-strain response at 0.072, 14.7, 28.8, 49.3 and 59.5 s^{-1} (Fig. 1a). The mechanical response observed at very high strain (> 300 %) reveals a hyperelastic material behavior with a strain rate sensitivity.

Then two testing machines are used to determine the compressive response of the SEBS gel at quasi-strain rates (0.0018, 0.018 and 0.18 s^{-1}) and intermediate strain rates (14.7, 28.8, 49.3 and 59.5 s^{-1}). Cylindrical samples of 10 mm in height and 5.5 mm in diameter are used to conduct experiments. Piezoelectric load cells and high-speed imaging contribute to the mechanical characterization. Indeed, above 40% in strain, imaging shows a barreling effect for quasi-static and intermediate strain rates experiments despite the use of a silicon oil lubricant at specimen/plates interfaces. Thus, Fig. 1b displays the gel mechanical response until 40% in strain in terms of engineering stress-strain curves from 0.0018 to 59.5 s^{-1}. As for tensile tests, the material exhibits a non-linear mechanical response with a strain rate dependence.

So as to reach strain rates consistent with the loading rate during blunt impact scenarios, Bracq et al. [22] have employed a compressive SHPB apparatus with polyamide bars. Actually, polyamide bars were chosen to match with the low impedance of the gel material. Full-bridge strain gauges were glued on the input and output bars in such a way to avoid the superposition of both incident and reflected waves. Moreover, typical recorded signals from strain gauges can be observed in Fig. 2. One can distinguish the incident wave $\varepsilon_I(t)$, the reflected wave $\varepsilon_R(t)$ and finally the transmitted wave $\varepsilon_T(t)$. However, the measured signals have to be rebuilt to consider viscoelastic effects of polyamide bars. Zhao and Gary [38] provide a 3D analytical solution for the longitudinal wave propagation in an infinite linear viscoelastic cylindrical bar based on a Fourier stationary harmonic wave analysis. This resolution is implemented in the DAVID® software used to determine the stress-strain response [39].

High-speed imaging has shown a non-homogeneous strain during experiments with the presence of a barreling effect and a radial strain wave propagating along the specimen axis. Therefore, Bracq et al. [22] have only expressed the stress-strain response in a nominal way for a range of strain rates from 490 to 1520 s^{-1} (see Fig 3a). To have an overview of the strain rate sensitivity of the SEBS gel, it has been decided to illustrate its engineering stress-strain response in compression until 40% in strain at quasi-static strain rates up to high strain rates (see Fig 3b). Dynamic curves at 490 and 1520 s^{-1} display oscillations

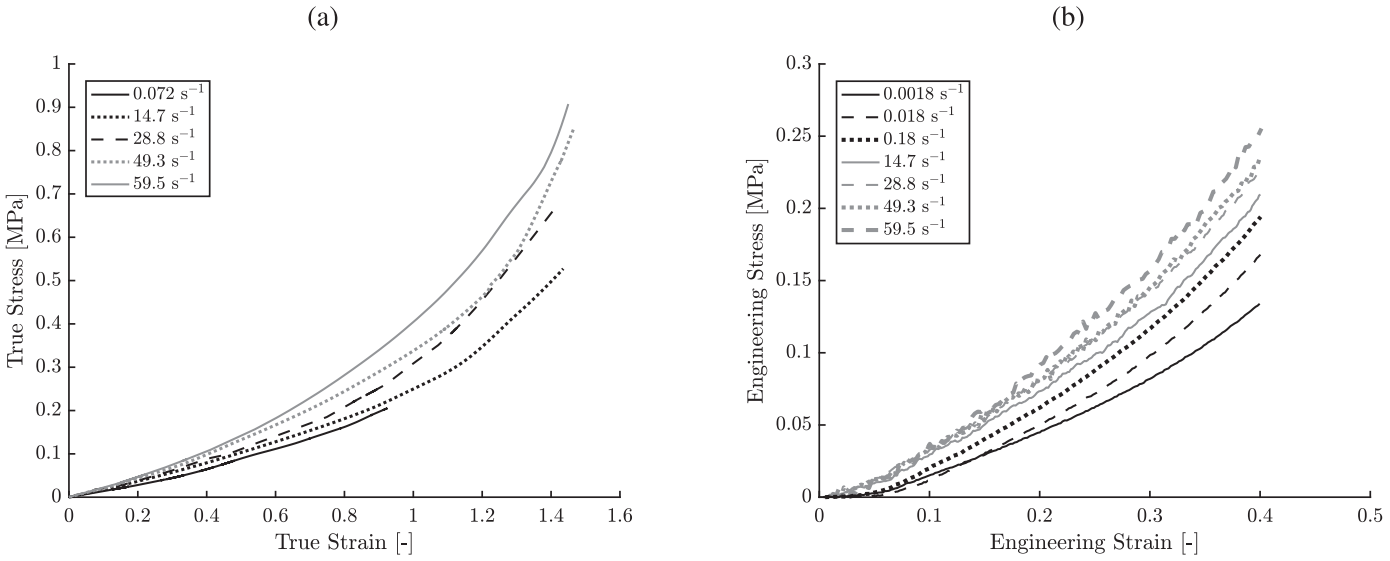

Fig. 1. True stress-strain curves determined from tensile tests at various strain rates (a) and engineering stress-strain curves determined from compressive tests at quasi-static and intermediate strain rates (b) [22].

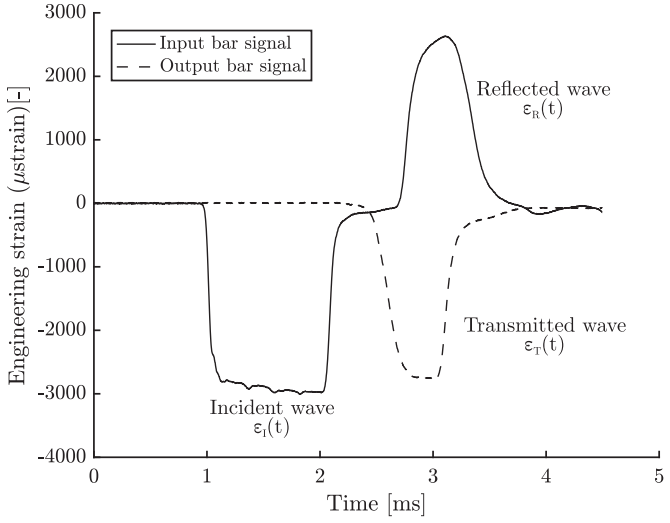

Fig. 2. Typical recording from strain gauges during dynamic compression testing [22].

which may be explained by the full-strain gauges sensitivity for low strain signals. Finally, the visco-hyperelastic material behavior is considered by means of a constitutive material law proposed in the next part.

4. Material model

Even though hyperelastic laws have already been implemented in many FE commercial software programs, the present authors choose to implement an extended hyperelastic law to take the strain rate sensitivity into account in a simple and reliable way. The explicit FE software Radioss (Altair HyperWorks) is employed for the modeling of dynamic impact events and the proposed law is implemented as a user material subroutine coded in Fortran. The Mooney–Rivlin material model [40] is adopted to represent the gel hyperelastic behavior. It is formulated based on the Ogden strain energy density function $W(\lambda_1, \lambda_2, \lambda_3)$ based on the principal stretch ratios λ_i.

The gel material forces the authors to model its behavior as a nearly incompressible material. Therefore, Holzapfel [41] mentions a multiplicative decomposition of the deformation gradient tensor **F** into deviatoric (volume preserving) and volumetric parts. This formulation leads to a modification of the strain energy density function W into deviatoric W_{dev} and volumetric W_{vol} components, depending on the modified principal stretch ratios $\overline{\lambda_i}$, and written as:

$$W(\overline{\lambda_1}, \overline{\lambda_2}, \overline{\lambda_3}, J) = W_{dev}(\overline{\lambda_1}, \overline{\lambda_2}, \overline{\lambda_3}) + W_{vol}(J) \tag{1}$$

where

$$W_{dev}(\overline{\lambda_1}, \overline{\lambda_2}, \overline{\lambda_3}) = \sum_{k=1}^{N} \frac{\mu_k}{\alpha_k}(\overline{\lambda_1}^{\alpha_k} + \overline{\lambda_2}^{\alpha_k} + \overline{\lambda_3}^{\alpha_k} - 3) \tag{2}$$

and

$$W_{vol}(J) = \frac{K}{2}(J-1)^2 \tag{3}$$

where J is the determinant of **F**. To reduce the Ogden model to a Mooney–Rivlin material model, specific values of material parameters are chosen (N = 2, $\alpha_1 = 2$, $\alpha_2 = -2$). The volumetric component is employed as a penalty approach to consider material incompressibility. K is the bulk modulus expressed as $K = 2\mu(1+\nu)/(3(1-2\nu))$. The shear modulus μ is calculated via $\mu = \sum_{k=1}^{N} \frac{\mu_k \alpha_k}{2}$. To avoid an infinite value for the bulk modulus and thus, a small time step in explicit simulations, a Poisson's ratio $\nu = 0.495$ is considered for the gel material improving numerical stability.

Two model parameters μ_1 and μ_2 must be calibrated based on mechanical experiments. In order to take the strain rate dependence of the material into account, the authors introduce two mathematical functions $\mu_1(\dot{\lambda_{eq}})$ and $\mu_2(\dot{\lambda_{eq}})$ depending on the equivalent engineering strain rate $\dot{\lambda_{eq}}$, defined as:

$$\dot{\lambda_{eq}} = \max_i(\dot{\lambda_i}),\ i = 1, 2, 3 \tag{4}$$

where $\dot{\lambda_i}$ are the time rate of variations of the principal stretch ratios λ_i ($i = 1, 2, 3$). Thus, the strain energy density function W now depends on the strain rate $\dot{\lambda_{eq}}$ and Eq. (2) may be written as:

$$W_{dev}(\overline{\lambda_1}, \overline{\lambda_2}, \overline{\lambda_3}, \dot{\lambda_{eq}}) = \sum_{k=1}^{N} \frac{\mu_k(\dot{\lambda_{eq}})}{\alpha_k}(\overline{\lambda_1}^{\alpha_k} + \overline{\lambda_2}^{\alpha_k} + \overline{\lambda_3}^{\alpha_k} - 3) \tag{5}$$

$\dot{\lambda_i}$ are obviously equivalent to engineering strain rates $\dot{\epsilon_i}$. Consequently, mechanical experiments performed at constant strain rates may be exploited in order to identify model parameters for each strain rate $\dot{\lambda_{eq}}$. Note that a strain rate filtering method is employed to reduce high frequency vibrations which are not physical. This improves

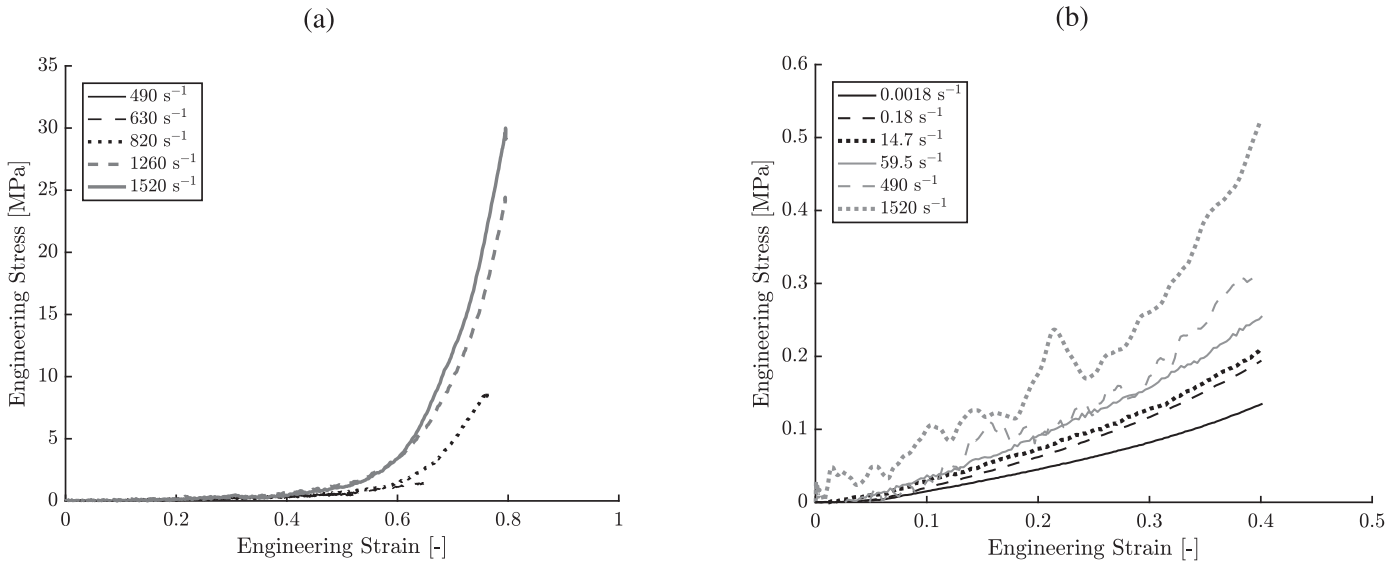

Fig. 3. Engineering stress-strain response during dynamic compressive tests at various strain rates (a) and strain rate influence on engineering stress-strain response at quasi-static to dynamic compressive experiments (b) [22].

the model stability and minimizes numerical artefacts. Moreover, the stability of the constitutive relation is preserved by keeping $\mu_1 > 0$ and $\mu_2 \leq 0$ [42].

5. Model parameters identification

In this section, the identification procedure of material model parameters is described, based on available mechanical experiments. In fact, the tensile material response is determined at quasi-static strain rate ($0.072\,s^{-1}$) up to intermediate strain rates ($59.5\,s^{-1}$). On the contrary, compressive experiments have been conducted at quasi-static strain rates up to dynamic strain rates. It means the tensile behavior of the SEBS gel at dynamic strain rates is unknown. The authors have consequently decided to examine the theoretical uniaxial stress σ_{xx} depending on the uniaxial stretch ratio λ_{xx} given by the Mooney–Rivlin model and described by Eq. (6) [41].

$$\sigma_{xx} = \mu_1\left(\lambda_{xx}^2 - \frac{1}{\lambda_{xx}}\right) + \mu_2\left(\frac{1}{\lambda_{xx}^2} - \lambda_{xx}\right) \tag{6}$$

Thus, σ_{xx} can be decomposed into two functions f and g in order to assess the influence of both material parameters μ_1 and μ_2 on loading modes (tension with $\lambda_{xx} > 1$ and compression with $\lambda_{xx} < 1$), as follows:

$$\sigma_{xx} = f(\mu_1, \lambda_{xx}) + g(\mu_2, \lambda_{xx}) \tag{7}$$

with,

$$\begin{cases} f(\mu_1, \lambda_{xx}) = \mu_1\left(\lambda_{xx}^2 - \frac{1}{\lambda_{xx}}\right) \\ g(\mu_2, \lambda_{xx}) = \mu_2\left(\frac{1}{\lambda_{xx}^2} - \lambda_{xx}\right) \end{cases} \tag{8}$$

Fig. 4 illustrates these two functions influencing the true stress by taking $\mu_1 = 1$ MPa and $\mu_2 = -1$ MPa. In fact, values of μ_1 and μ_2 have to be chosen in order to ensure a positive shear modulus and material stability. Through this figure, it can be emphasized that the function f related to μ_1 governs the behavior in tension in contrast with the function g related to μ_2 governing the behavior in compression. It means a small change in μ_2 will alter the compressive material response while minimizing its effect on tension. Based on this conclusion and experimental data, μ_1 is identified through quasi-static tests performed in tension and compression with $\mu_2 = 0$ MPa. Thus, the model considers the non-linear behavior of the material in both tensile and compressive loadings. Then μ_2 is identified for each compressive strain rate testing.

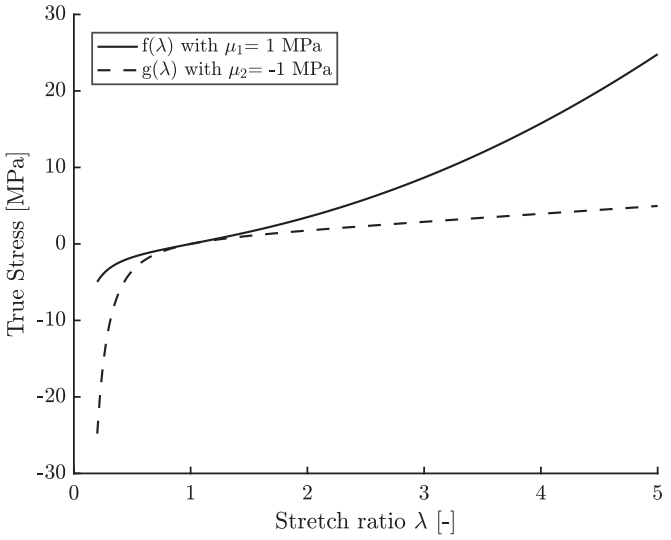

Fig. 4. Plots of functions $f(\mu_1, \lambda_{xx})$ and $g(\mu_2, \lambda_{xx})$ influencing the uniaxial true stress of a Mooney–Rivlin material model.

The choice to make only μ_2 strain rate sensitive minimizes its influence on tensile response which is unknown at dynamic strain rates. It also simplifies the parameters' identification procedure described thereafter.

5.1. Direct identification from quasi-static experiments

Firstly, one parameter material model is considered. Stress-strain curves at quasi-static strain rates are analyzed to identify the model parameter μ_1. Indeed, experiments at the lowest strain rates mean $0.072\,s^{-1}$ in tension (Fig. 1 a) and $0.0018\,s^{-1}$ in compression (Fig. 1b) are used to identify the μ_1 parameter. Axial and homogeneous loading conditions are ensured during tensile tests. Similarly, these conditions are preserved during compressive tests until 40% in strain. The material response in tension and compression at the lowest strain rates are exploited to correlate with σ_{xx} (Eq. (6)) based on the Levenberg–Marquardt (LM) algorithm with the MATLAB Curve Fitting Toolbox (MathWorks). A unique μ_1 coefficient independent of the strain rate is thus determined with $\mu_1 = 0.0434$ MPa. The goodness of the fit is evaluated with a R-squared coefficient of determination equal to

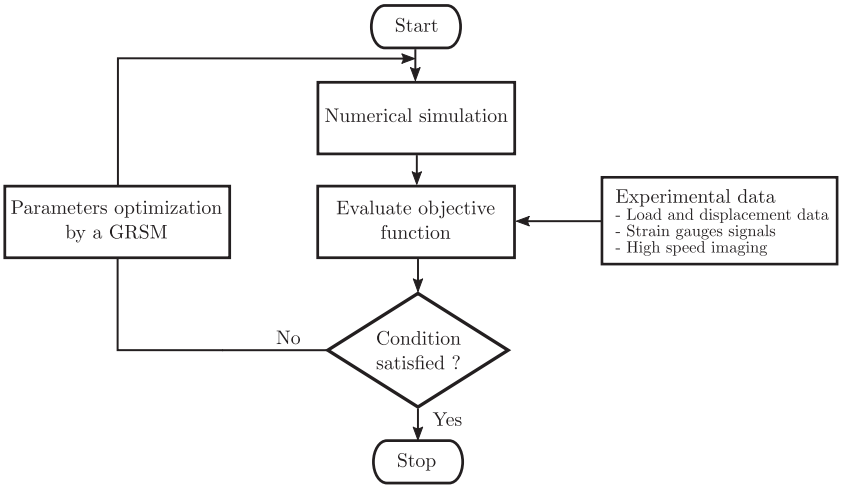

Fig. 5. Flow chart for numerical solving of an inverse problem.

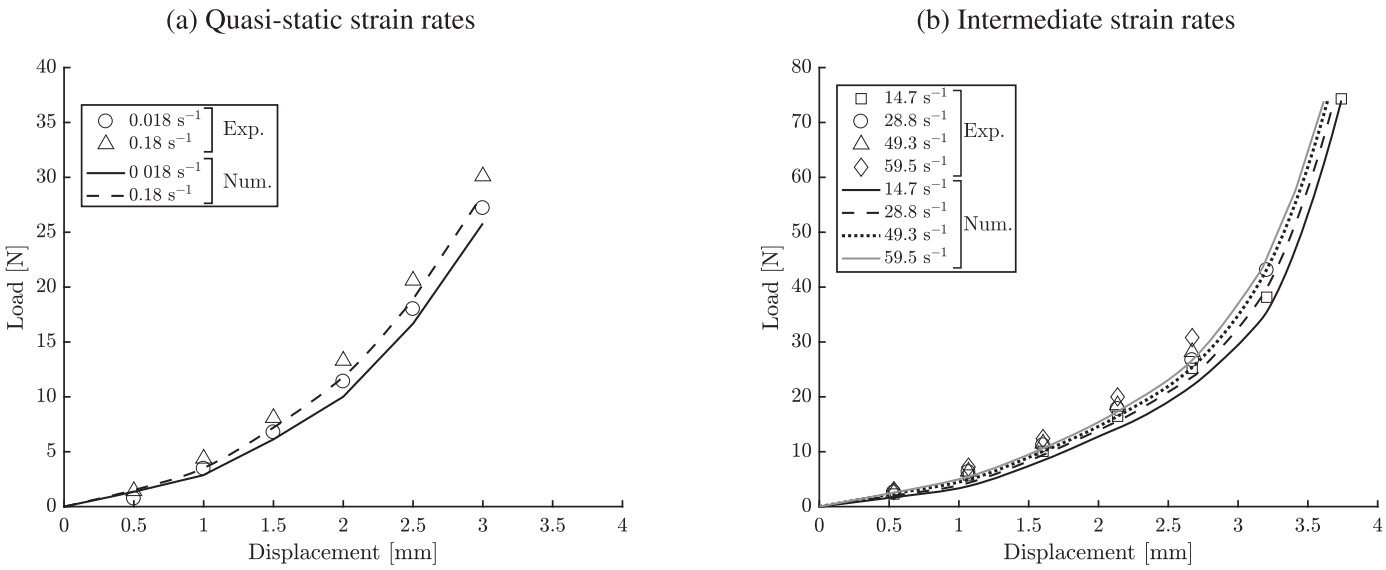

Fig. 6. Experimental and numerical load-displacement curves during compressive tests at quasi-static strain rates (a) and at intermediate strain rates (b).

0.9444.

5.2. Indirect identification from compressive experiments

An inverse technique is used to identify the model parameters (see Fig. 5). It is based on the accurate FE modeling of compression experiments for quasi-static, intermediate and high strain rates configurations. Indeed, it may reproduce the non-homogeneous strain and the barreling effect observed experimentally. Experimental data with load and displacement curves, strain gauge signals and high-speed imaging are exploited to fit numerical responses. The optimization procedure to identify model parameters is conducted with the HyperStudy optimization software (Altair HyperWorks) as a least square problem. Hence, experimental and numerical data, respectively X_{exp} and X_{num} at several sampling points N, are evaluated. Thus, the least square error e is introduced with Eq. (9):

$$e = \sum_{k=1}^{N} (X_{exp}^{k} - X_{num}^{k})^2 \tag{9}$$

Minimizing e through a global response surface method (GRSM) leads to the identification of model parameters. μ_2 parameter turns out to be the only parameter depending on the strain rate and may be identified afterwards through the modeling of compressive tests and an optimization software.

The commercial software HyperMesh (Altair HyperWorks) is employed to replicate all compressive experiments numerically. For each configuration, under-integrated hexahedral elements with physical stabilization are chosen along with a total strain formulation. Moreover, a mesh convergence is initially investigated to obtain a trade off between accuracy of results and computing costs.

Quasi-static and intermediate strain rates experiments are modeled first of all. Indeed, for these tests, equivalent loading conditions are applied to the sample. A fixed steel plate is used to support the sample and another one to compress it. Therefore, consistent boundary conditions are set up with experimental displacement rates applied to the movable plate. To correctly model experimental contact conditions, surface-to-surface general contact interface (TYPE 19) with a simple Coulomb friction law is employed. The same friction coefficient $F_{Coulomb}$ is used for the two contact gel/plates interfaces. This coefficient, involved in the deformation response, is added as a variable in the parameters' identification process. In addition, a sensitivity study is conducted to define consistent boundary values for the friction coefficient during the optimization process. High-speed imaging, load and displacement data over time are used as objectives to reach in the optimization procedure. Once the objective function has converged to its

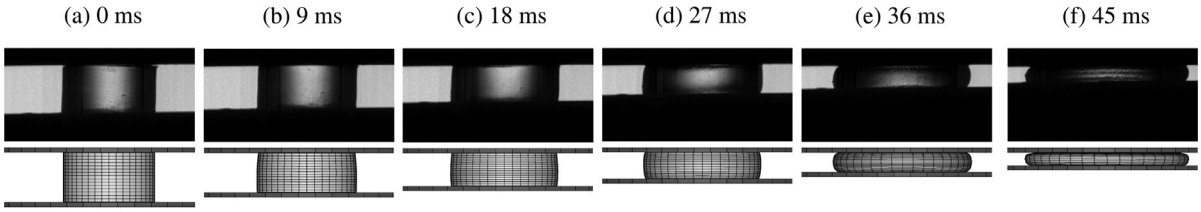

Fig. 7. Evolution of experimental and numerical sample deformation during compressive testing at 14.7 s^{-1}.

Table 1
Optimized model parameters during modeling of compressive experiments at quasi-static and intermediate strain rates.

Strain rate [s^{-1}]	0.018	0.18	14.7	28.8	49.3	59.5
μ_1 [MPa]			0.0434[a]			
μ_2 [MPa]	−0.0055	−0.0077	−0.0097	−0.0117	−0.0128	−0.0137
$F_{Coulomb}$ [-]			0.06[a]			

[a] Constant for all strain rates.

Table 2
Split Hopkinson Pressure Bar characteristics.

	Striker bar	Input bar	Output bar
Length (mm)	950	3040	3020
Diameter (mm)	16.1	20.3	20.4
Density (kg/m^3)	1149	1158	1146
Wave speed (m/s)	1750	1740	1740
Young modulus (MPa)	3517	3506	3470
Poisson's ratio	0.4	0.4	0.4

minimum value for each strain rate, experimental and numerical responses may be compared. Indeed, Fig. 6 depicts compressive experimental and numerical load-displacement curves for quasi-static and intermediate strain rates. It highlights a satisfactory correlation considering a two parameters material model. The ability of the constitutive law to replicate the deformation shape can also be seen in Fig. 7. Experimental and numerical sample deformation as well as the mesh discretization may be observed during a compressive test performed at a constant strain rate of 14.7 s^{-1}. In this range of strain rates, a constant friction coefficient is sufficient to correlate with experimental results. The relatively low value of the friction coefficient is consistent with the use of silicon oil lubricant at specimen/bar interfaces. Hence, it validates the identification procedure and optimized parameters values are resumed in Table 1 at quasi-static and intermediate strain rates.

So as to numerically replicate dynamic experiments using the SHPB apparatus in a reliable way, it has been decided to perform a full FE model from the striker to the output bar (see Fig. 8). Moreover, symmetry planes are used to obtain a quarter of the 3D FE model. The striker bar initial velocity V_0 measured experimentally is imposed on the numerical one. Fig. 8 also indicates the mesh discretization near strain gauges as well as for the sample. Additionally, elements in red are used to record input (Fig. 8a) and output (Fig. 8c) strain signals in the x direction. Contact interfaces are handled with the surface-to-surface general contact interface (TYPE 19). A Coulomb friction law is introduced between specimen/bar interfaces and a minimal gap is chosen for convenient numerical solving. Indeed, the barreling effect and the particular deformation pattern observed experimentally result in the use of a friction law in the FE model. As the previous configuration, an identical friction coefficient $F_{Coulomb}$ is used for both sides of the sample.

In fact, a previous study mentioned the use of a constant friction coefficient in numerical simulation of SHPB experiments [43]. In the present study, a constant friction coefficient is used for simplicity and quantifies the average friction between sample/bars interfaces. Dimensions and mechanical properties of each polymeric bar are resumed in Table 2. An ultrasound device (EPOCH LT) is used to measure the longitudinal wave speed of nylon and gel samples.

Transmitted strain signals and high-speed imaging data for each dynamic strain rate are used as objectives to reach in the optimization process. Furthermore, the Coulomb friction coefficient $F_{Coulomb}$ is also a parameter to identify through the inverse technique. Once the optimization procedure is accomplished for each strain rate, recorded experimental and numerical strain signals from input and output bars can be compared. On the one hand, Fig. 9 highlights the excellent correlation of experimental and numerical incident waves (under the solid axis and dotted gray lines) for each strain rate. Hence, it validates the mechanical properties identified for Hopkinson bars. On the other hand, it shows a very satisfactory match between experimental and numerical output signals, i.e. transmitted signals. More precisely, numerical output signals are identified over a specific period of time. Indeed, considering the traveling of the transmitted wave, a specific moment during the output signal raise refers to a certain axial sample deformation. Therefore, the period of identification is calculated until the sample diameter reaches the bars' diameter. As elements are subjected to very compressive strains (more than 80%) and considering the material's incompressible nature, the sample diameter gradually increases until it exceeds the bars' diameter. Sample elements are exposed to very high distortions after this specific instant, leading to higher and unrealistic stress inside the specimen. Consequently, it may explain why numerical output strain signals are slightly inferior to experimental

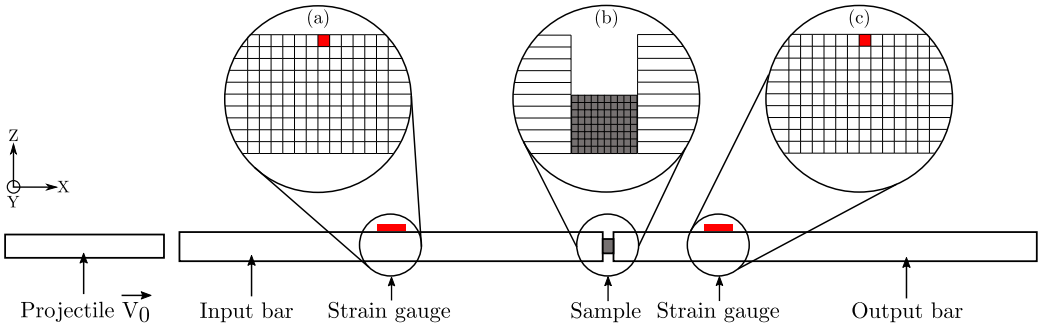

Fig. 8. Representation of the FE mesh for the modeling of SHPB experiments.

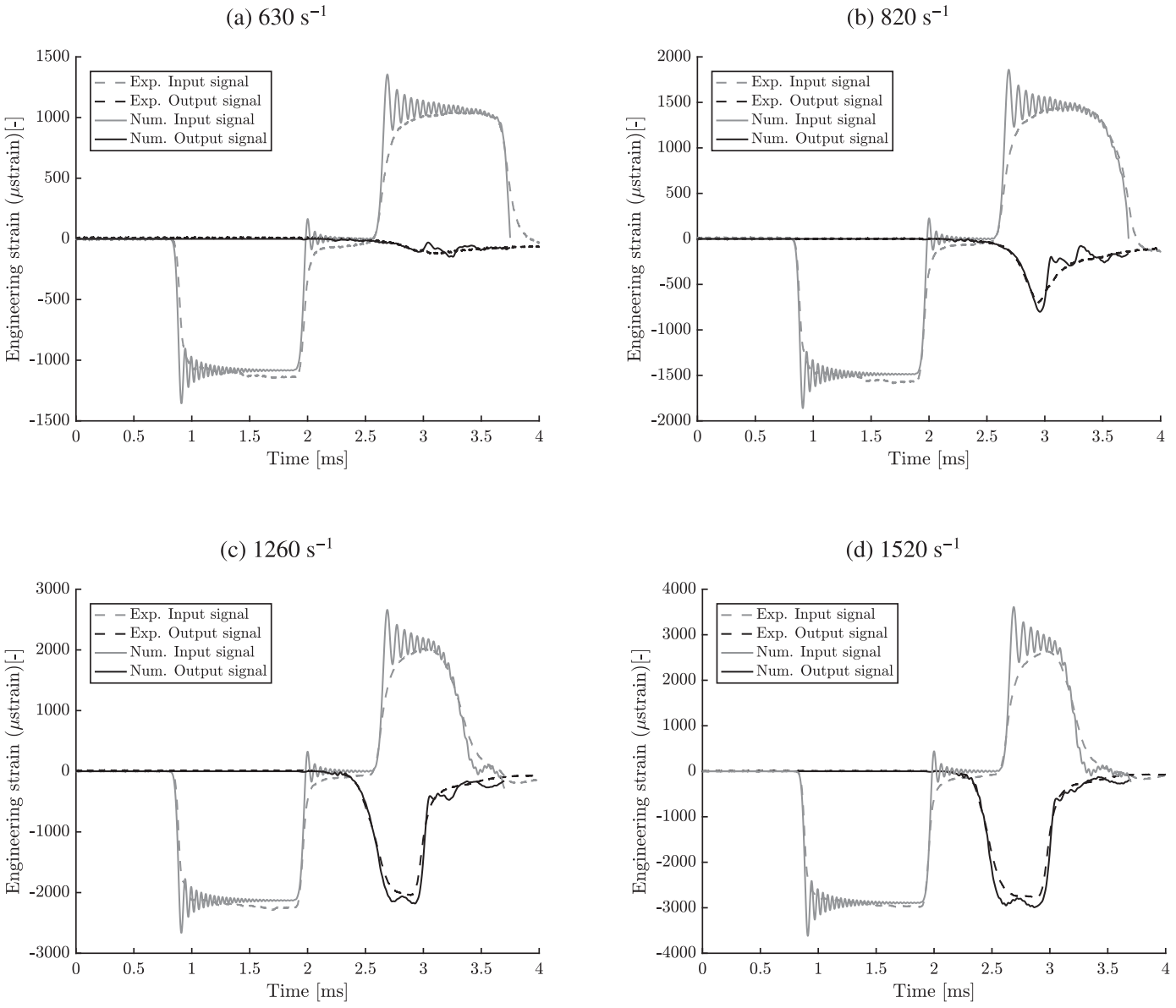

Fig. 9. Correlation of experimental and numerical strain as a function of time from input and output strain gauges for various dynamic strain rates.

ones for Fig. 9c and d. For lower strain rates, this observation is not made because the sample diameter remains under the bars' diameter. One can notice that numerical results related to the dynamic experiment performed at 490 s^{-1} are not presented. Actually, the low signal to noise ratio obtained for the numerical transmitted signal prevents the authors from identifying reliable parameters.

Moreover, the evolution of the experimental and numerical sample deformation during dynamic compressive testing at 1520 s^{-1} can be observed in Fig. 10. It results in the FE model's ability to reproduce loading and friction conditions as well as the gel deformation. Furthermore, Fig. 10f depicts the very high element deformation and defines the comparison limits. The use of high-speed imaging during dynamic tests highlights the non-homogeneous strain at the early stages of the deformation and thus an unstable strain rate [22]. As the material exhibits a very low stiffness at low strains, it does not invalidate the assumption of a constant strain rate. Indeed, a steady strain rate is

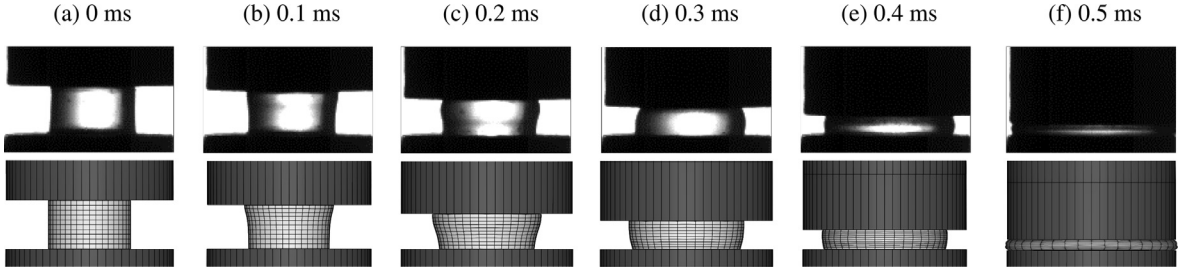

Fig. 10. Evolution of experimental and numerical sample deformation during dynamic compressive testing at 1520 s^{-1}.

Table 3
Optimized model parameters during modeling of compressive experiments at dynamic strain rates.

Strain rate [s^{-1}]	630	820	1260	1520
μ_1 [MPa]		0.0434[a]		
μ_2 [MPa]	−0.0176	−0.0241	−0.0255	−0.0268
$F_{Coulomb}$ [-]	0.0504	0.0322	0.0246	0.0223

[a] Constant for all strain rates.

obtained during the major part of the deformation range. Values of μ_2 and $F_{Coulomb}$ are then determined for each dynamic strain rate and are resumed in Table 3. This shows that the friction coefficient decreases when the strain rate increases and indeed, it is commonly known that the friction coefficient relies upon the relative velocity between two contact surfaces. As the kinetic friction coefficient is generally smaller than the static one, it is compatible with the values of friction coefficient obtained for each strain rate [43,44].

The identification of the μ_2 parameter completed for each strain rate contributes to the determination of a power-law based trend function depending on the strain rate with the use of the Levenbergh–Marquardt algorithm (MATLAB Curve Fitting Toolbox, MathWorks). Fig. 11 depicts the parameters' data as well as the identified power law. The R-squared coefficient of determination obtained comforts the authors in the establishment of such a function. Another way to depict how the proposed material model handles the strain rate sensitivity is through Fig. 12. Indeed, the uniaxial material response is given for various strain rates based on both Eq. (6) and parameters' values (see Tables 1 and 3). In addition, it may be noted that the strain rate dependence mainly affects compressive loading modes. On the contrary, the tensile behavior is slightly influenced by the strain rate which is the purpose of the identification procedure. The visco-hyperelastic law using the trend function determined previously is implemented in Radioss explicit code (Altair HyperWorks) and is validated afterwards through comparisons of numerical blunt ballistic impacts with experimental ones at diverse projectile velocities.

6. Modeling of blunt ballistic experiments and validation

Before carrying out impact modeling, it is crucial to perform reliable and repeatable non-penetrating impacts. Real-world impact events may be replicated on a 25 cm gel block cube as these dimensions avoid the influence of edge effects on the gel wall displacement. Fig. 13a represents the experimental set-up for ballistic impact studies. Projectiles

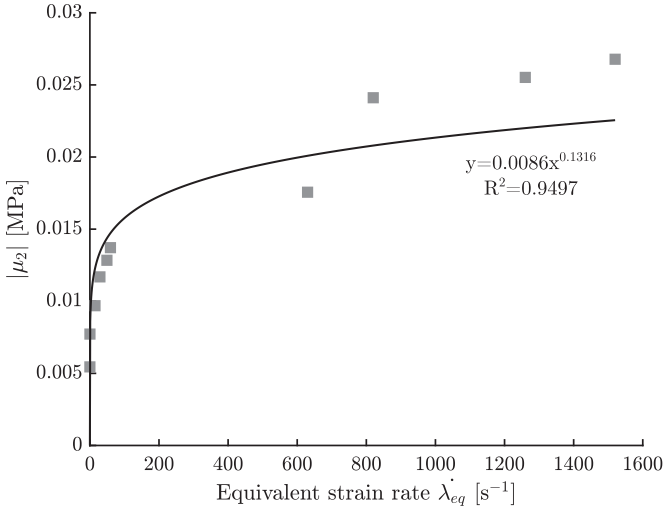

Fig. 11. Model parameter value versus the strain rate and its power fitting function.

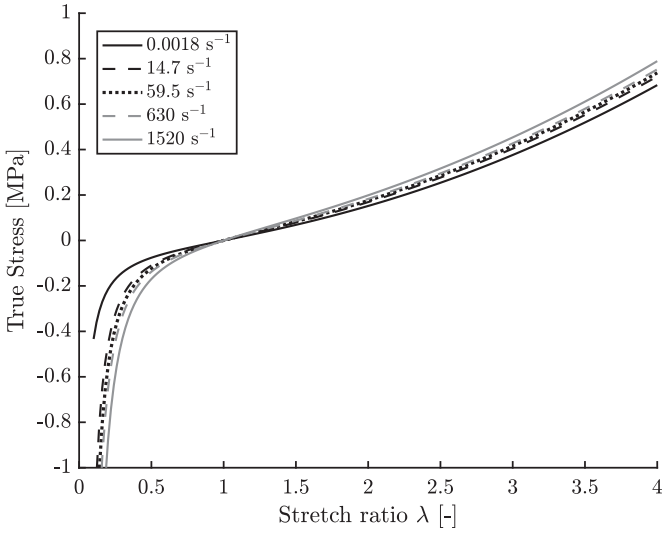

Fig. 12. Uniaxial material response of the visco-hyperelastic law for various strain rates.

are placed in a pneumatic launcher in a way to strike the gel center. A velocity sensor at the barrel nozzle exit measures the projectile velocity and pressure can be adjusted to obtain the desired projectile speed. A lighting device and a high-speed camera are jointly used to capture the ballistic event. Transparent light rulers are fixed to the gel surface, leading to the precise measurement of the dynamic gel wall displacement in both horizontal and vertical directions. Fig. 13b is a photograph of the gel wall displacement during the impact of a rigid round projectile of 37 mm in diameter and a mass of 140 g launched at 20 m/s. The same projectile is employed by Bir et al. [6]. This study corresponds to one of the most complete investigations about the impact of LLKE projectiles on PMHS'sternum with an aim of injury criteria assessment. A dedicated routine is used to perform a digital image correlation using black and white contrast (white dotted line in Fig. 13b) capturing gel wall displacements.

One of the principal measurements during ballistic impacts is the highest gel wall displacement over time. The repeatability and the material ability to return to its initial state after an impact event are ensured by conducting multiple ballistic tests for each impact condition. For instance, Fig. 14 represents the gel wall displacement time history for five tests corresponding to the impact of the Fig. 13b at 20 m/s. It results in the validation of experimental testing with a relative displacement error less than 3.5%.

FE modeling of blunt ballistic experiments is conducted by firstly studying the mesh convergence for the gel block as in the previous section. Simulating a non-penetrating impact results in very high elements distortion. Hence, important efforts have to be made to propose a suitable FE model. A fine mesh is preferred at the region of impact and a coarser mesh size is chosen further away from impact location. The FE discretization of the gel for each direction is depicted as well as the block dimensions in Fig. 15. To be consistent with the experimental set-up presented in Fig. 13a, the top and sides of the FE gel block can be left free. Due to very fast impact events, the numerical model can be simplified by leaving the downside of the FE gel block free. These boundary conditions reduce the model to a quarter by symmetry planes. Moreover, the backing plate employed during impact testing is numerically considered by fixing a null displacement for the backing nodes of the FE gel block. The complete boundary conditions applied to the gel block are illustrated in Fig. 15. The projectile used during impact testing is modeled as rigid. As for previous numerical studies, the surface-to-surface general contact interface is chosen to model projectile/gel contact. However, the friction effect is not considered during impact modeling. Indeed, a sensitivity analysis of the friction coefficient is

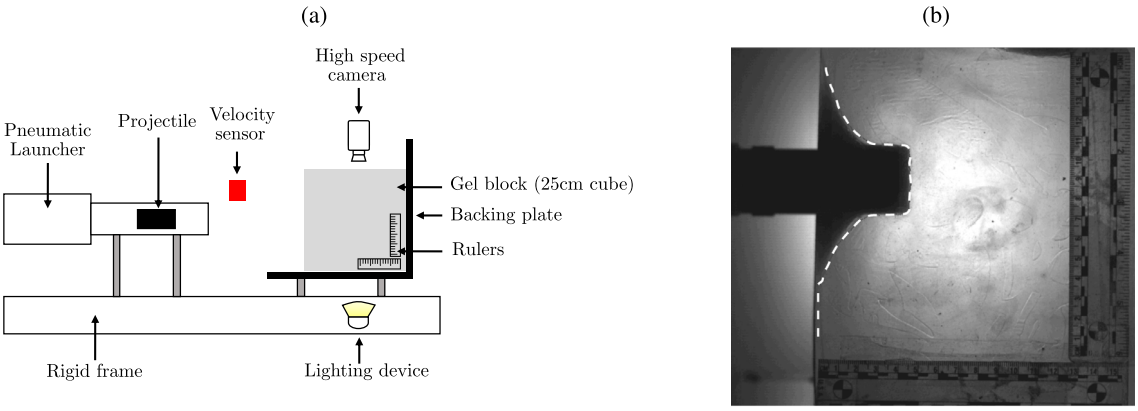

Fig. 13. (a) Schematics of the experimental set-up for ballistic impact studies and (b) a photograph of the gel wall displacement during the impact of a rigid projectile.

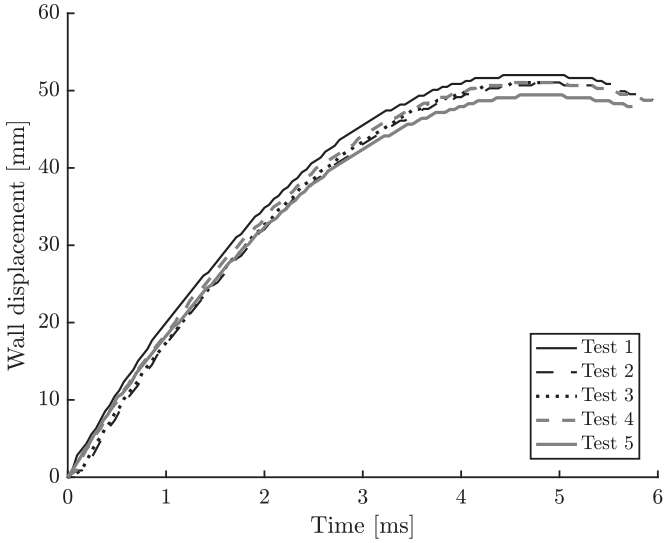

Fig. 14. Gel wall displacement versus time for five non-penetrating ballistic impacts on a gel block for a projectile velocity of 20 m/s.

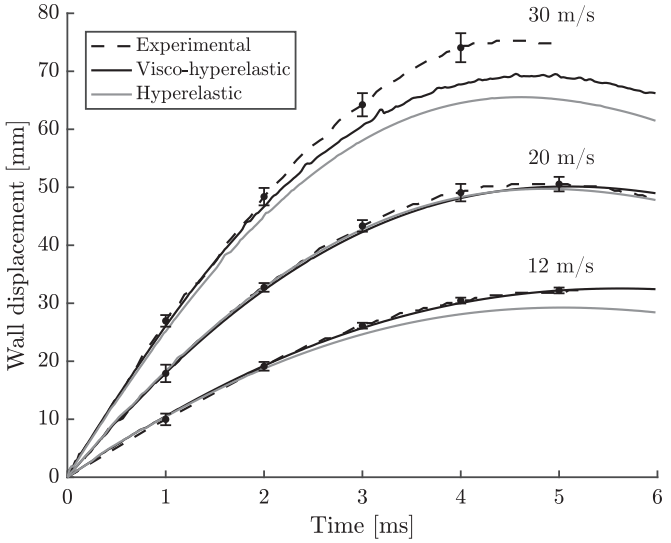

Fig. 16. Experimental and numerical gel wall displacement as a function of time at diverse impact velocities.

undertaken and reveals it to be irrelevant for the numerical study. It has no influence on the gel wall displacement profile as it is a macroscopic metric.

Three impact conditions are replicated on the gel block with the projectile initial velocities of 12, 20 and 30 m/s. Moreover, to highlight the necessity of taking the material strain rate sensitivity into account, a simple Mooney–Rivlin hyperelastic material model is compared to the proposed model. The parameters are in this case identified by an inverse method using experimental wall displacement data for an initial velocity of 20 m/s. These parameters are then used to model the impact at 12 and 30 m/s. Fig. 16 presents the experimental and numerical gel wall displacement versus time for 12, 20 and 30 m/s. Firstly, error bars illustrate the reduced scattering of experimental measurements for the three velocities with a relative error less than 4%. Secondly, Fig. 16 highlights the very satisfactory correlation of the proposed visco-hyperelastic model compared to experimental curves. Thirdly, the model developed provides a better accuracy than a simple hyperelastic model. Moreover, it is important to note that the proposed model is based on material physical properties. In addition, Fig. 16 depicts that for 30 m/s, the FE model is less precise at very high displacements and thus, very

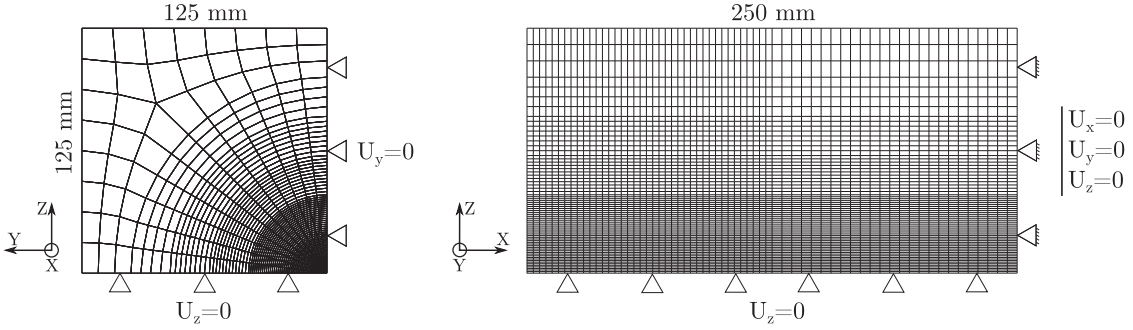

Fig. 15. Representation of the FE mesh for the gel block during the modeling of blunt ballistic impacts.

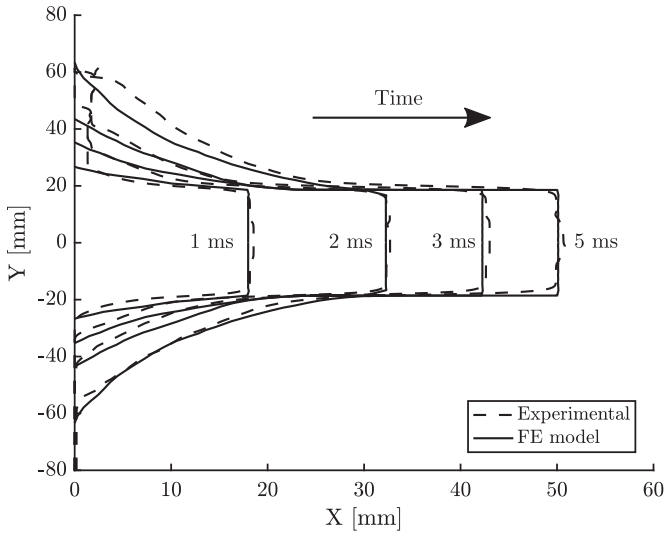

Fig. 17. 2D gel wall displacement profiles for experimental and numerical impacts at diverse moments for an impact at 20 m/s.

high elements distortions show the limits of FE modeling.

The ability of the FE model to obtain an accurate dynamic gel displacement profile during an impact event is exhibited in Fig. 17. Indeed, it presents the evolution of the 2D displacement profile of the gel wall over time. It corresponds to the impact of a rigid projectile launched at 20 m/s. Predicted profiles at 1, 2, 3 and 5 ms demonstrate excellent agreements with measured ones. Some discrepancies can still be observed between experimental and numerical profiles for a vertical position $Y > 40$ mm. It may be explained by non-perfect symmetrical impact conditions against numerical ones which are ideal. Furthermore, the 2D displacement profile leads to the calculation of the displaced volume at all times for the three impact conditions: 12, 20 and 30 m/s. Indeed, cylindrical projectiles provide a symmetric deformation. Hence, the displaced volume can be determined by integrating the 2D displacement profile. Fig. 18 depicts the measured and predicted displaced volume over time at diverse impact velocities. Volumes determined numerically are in excellent agreement with experimental results for 12 and 20 m/s. At 30 m/s, some discrepancies appear at about 4 ms. This moment is related to the higher error introduced by the numerical model in terms of gel wall displacements (see Fig. 16). Furthermore,

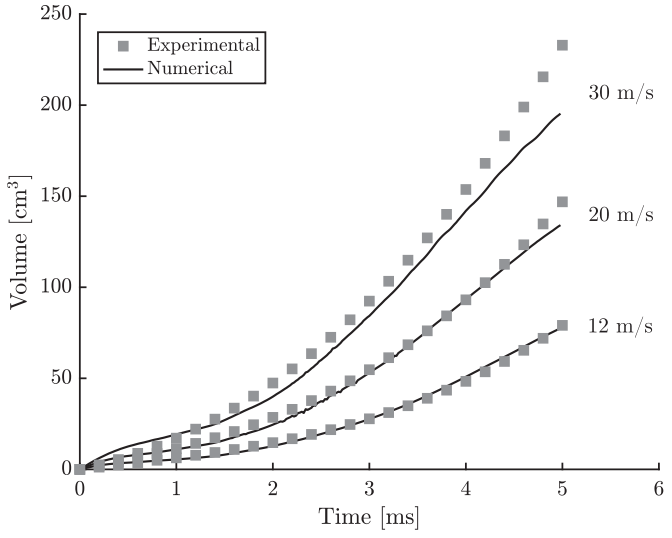

Fig. 18. Measured and predicted displaced volume as a function of time at diverse impact velocities.

disparities at low displaced volumes can be explained by the difficulty of capturing gel displacements at the beginning of impacts due to optical issues.

Qualitative comparisons may also be introduced between experimental and numerical displacement profiles during a non-penetrating ballistic event. Fig. 19 illustrates the evolution of the gel wall displacement observed experimentally and numerically for an impact at an initial velocity of 20 m/s. Fig. 19a–f demonstrate the FE model's ability to predict the dynamic gel wall displacement during a blunt ballistic impact. It is worth noting that elements are subjected to very high strains in front of the projectile. In addition, this projectile with sharp edges increases elements distortion (see Fig. 19f). Therefore, a less complex deformation is expected by impacting curved projectiles or modeling behind armor deformation. The loading mode being mainly compression, it sustains the experimental and numerical study of the gel behavior over a wide range of strain rates.

7. Conclusions

A new visco-hyperelastic constitutive law has been developed for a polymer gel to analyze blunt ballistic impacts. It is based on the two parameters of the Mooney–Rivlin material model depending on principal stretch ratios. Furthermore, the strain rate dependence is taken into account by determining model parameters for each strain rate.

The determination of model parameters relies on a specific identification procedure. Indeed, a previous study on the mechanical characterization of the SEBS gel through tensile and compressive tests led to the establishment of a direct and indirect identification technique. Moreover, the tensile response of the gel at dynamic strain rates is unknown consequently impacting the proposed approach.

On the one hand, the authors attempt to minimize the strain rate sensitivity for tensile loadings by the identification of one strain rate independent material parameter. It is identified by means of tensile and compressive experiments performed at a quasi-static strain rate. This rate of deformation ensures stress equilibrium and a homogeneous strain.

On the other hand, an optimization by inverse technique is necessary to identify the second parameter through the modeling of compressive tests for each experimental configuration. The experimental study shows complex loading modes with the presence of a barreling effect and a non-homogeneous strain. The optimization software HyperStudy is used along with the explicit code Radioss (Altair HyperWorks) to simulate compressive experiments and identify model parameters. More precisely, a multi-objective optimization using the response surface method is employed to fit model results with experimental ones. For this purpose, high-speed imaging, load and displacement data are exploited. To replicate the observed deformation numerically, a Coulomb friction law is introduced to capture the mean friction between specimen/plates interfaces. In addition, this coefficient is also identified with the optimization procedure. The comparison of experimental and numerical results indicates the FE model's ability to capture the precise material response subjected to compressive loadings over a wide range of strain rates. Moreover, the strain rate dependence of the model parameter is fitted with a power law based function giving excellent correlation. The proposed visco-hyperelastic model is therefore implemented as a user-material subroutine in Radioss software.

The constitutive law developed in this paper is validated against the FE modeling of blunt ballistic experiments. A rigid projectile is impacted at various velocities on the gel block. FE model results demonstrate very satisfactory responses through comparison with experiments. Indeed, the model exhibits both an accurate gel wall displacement and a consistent dynamic deformation. Moreover, this study highlights the necessity to take the strain rate sensitivity of the material into account by comparing the model developed with a simple hyperelastic model calibrated at a specific projectile velocity. However, for a very high gel wall displacement, the FE model is less

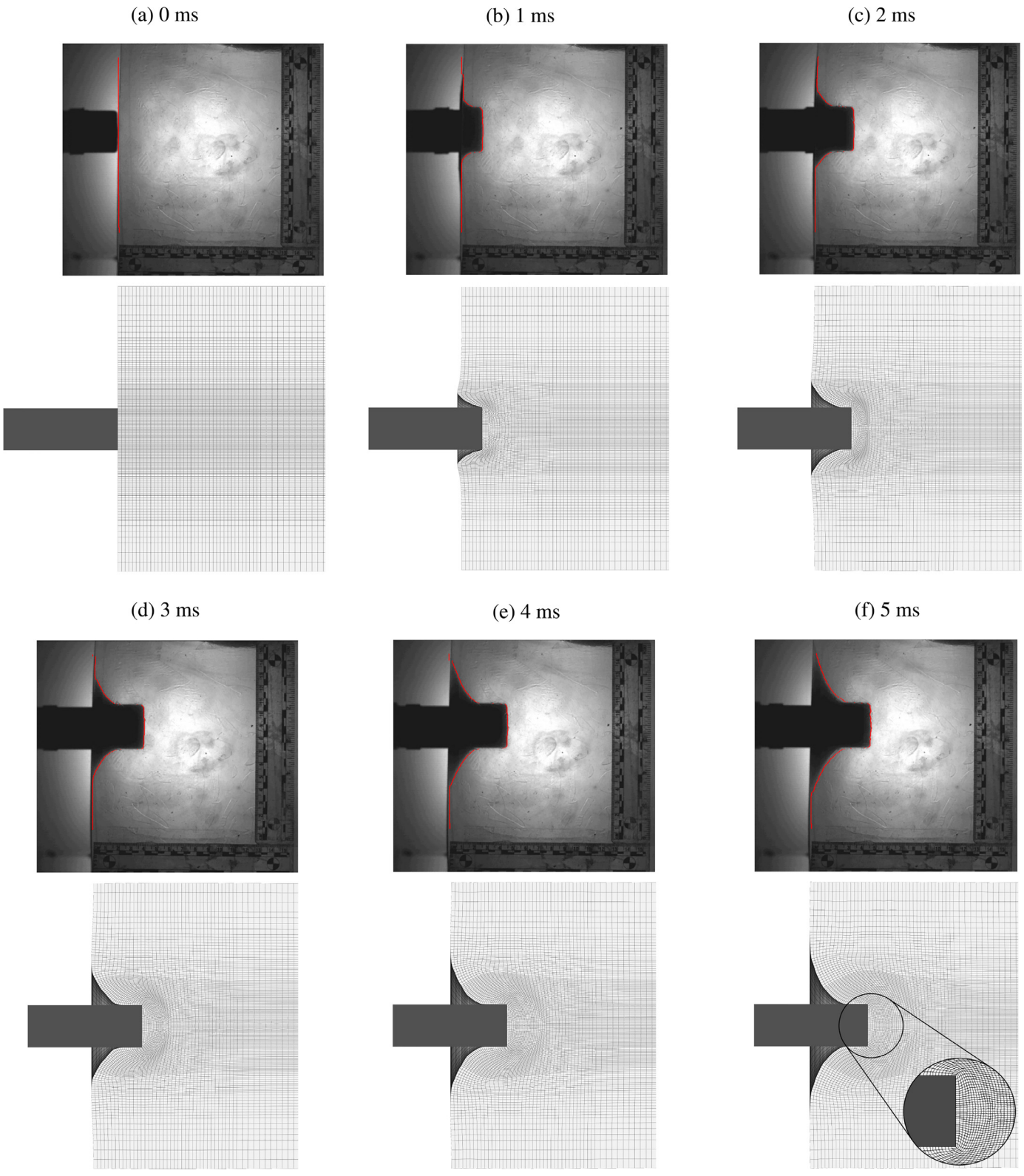

Fig. 19. Evolution of experimental and numerical gel displacement profiles due to a blunt ballistic impact at an initial impact velocity of 20 m/s.

representative, probably due to important elements distortion. The smoothed particle hydrodynamics method may then be introduced to go further with the modeling of non-penetrating ballistic impacts.

Finally, this study may lead to subsequent investigations on blunt ballistic impacts and gives insight into blunt ballistic trauma with the use of a homogeneous target medium (SEBS gel block) and a human torso FE model [45].

Acknowledgments

This research is funded by the French Ministry of the Interior and is carried out within the framework of the CNRS Research Federation on

Ground Transports and Mobility, in articulation with the ELSAT2020 project supported by the European Community, the French Ministry of Higher Education and Research, the Hauts de France Regional Council, The AIP-Priméca Nord-Pas de Calais group. The authors gratefully acknowledge the support of these institutions.

Supplementary material

Supplementary material associated with this article can be found, in the online version, at 10.1016/j.ijimpeng.2018.04.001.

References

[1] Ritchie AJ. Plastic bullets: significant risk of serious injury above the diaphragm. Injury 1992;23(4):265–6. http://www.sciencedirect.com/science/article/pii/S0020138305800130.

[2] de Brito D, Challoner KR, Sehgal A, Mallon W. The injury pattern of a new law enforcement weapon: the police bean bag. Ann Emergency Med 2001;38(4):383–90. http://dx.doi.org/10.1067/mem.2001.117272. http://linkinghub.elsevier.com/retrieve/pii/S0196064401722512.

[3] Suyama J, Panagos PD, Sztajnkrycer MD, FitzGerald DJ, Barnes D. Injury patterns related to use of less-lethal weapons during a period of civil unrest. J Emergency Med 2003;25(2):219–27. http://dx.doi.org/10.1016/S0736-4679(03)00179-3. http://linkinghub.elsevier.com/retrieve/pii/S0736467903001793.

[4] Wahl P, Schreyer N, Yersin B. Injury pattern of the flash-ball, a less-lethal weapon used for law enforcement: report of two cases and review of the literature. J Emergency Med 2006;31(3):325–30. http://dx.doi.org/10.1016/j.jemermed.2005.09.022. http://linkinghub.elsevier.com/retrieve/pii/S0736467906004914.

[5] Kobayashi M, Mellen PF. Rubber bullet injury: case report with autopsy observation and literature review. Am J Forensic Med Pathol 2009;30(3):262–7. http://dx.doi.org/10.1097/PAF.0b013e318187dfa8. http://content.wkhealth.com/linkback/openurl?sid=WKPTLP:landingpage&an=00000433-200909000-00010.

[6] Bir C, Viano D, King A. Development of biomechanical response corridors of the thorax to blunt ballistic impacts. J Biomech 2004;37(1):73–9. http://dx.doi.org/10.1016/S0021-9290(03)00238-0. http://linkinghub.elsevier.com/retrieve/pii/S0021929003002380.

[7] Pavier J, Langlet A, Eches N, Prat N, Bailly P, Jacquet J-F. Experimental study of the coupling parameters influencing the terminal effects of thoracic blunt ballistic impacts. Forensic Sci Int 2015;252:39–51. http://dx.doi.org/10.1016/j.forsciint.2015.04.004. http://linkinghub.elsevier.com/retrieve/pii/S0379073815001504.

[8] Prat N, Rongieras F, de Freminville H, Magnan P, Debord E, Fusai T, et al. Comparison of thoracic wall behavior in large animals and human cadavers submitted to an identical ballistic blunt thoracic trauma. Forensic Sci Int 2012;222(1–3):179–85. http://dx.doi.org/10.1016/j.forsciint.2012.05.022. http://linkinghub.elsevier.com/retrieve/pii/S0379073812002708.

[9] Bresson F, Ducouret J, Peyre J, Marechal C, Delille R, Colard T, et al. Experimental study of the expansion dynamic of 9mm Parabellum hollow point projectiles in ballistic gelatin. Forensic Sci Int 2012;219(1–3):113–8. http://dx.doi.org/10.1016/j.forsciint.2011.12.007. http://linkinghub.elsevier.com/retrieve/pii/S0379073811005998.

[10] Swain M, Kieser D, Shah S, Kieser J. Projectile penetration into ballistic gelatin. J Mech Behav Biomed Mater 2014;29:385–92. http://dx.doi.org/10.1016/j.jmbbm.2013.09.024. http://linkinghub.elsevier.com/retrieve/pii/S1751616113003251.

[11] Metker LW, Prather RN, Johnson EM. A method for determining backface signatures of soft body armors. Ft. Belvoir: Defense Technical Information Center; 1975. http://handle.dtic.mil/100.2/ADA012797.

[12] Police body armor standards and testing, volume II: appendices. Tech. Rep. OTA-ISC-535. Washington, DC: U.S. Government Printing Office: U.S. Congress, Office of Technology Assessment; 1992.

[13] Liu L, Fan Y, Li W. Viscoelastic shock wave in ballistic gelatin behind soft body armor. J Mech Behav Biomed Mater 2014;34:199–207. http://dx.doi.org/10.1016/j.jmbbm.2014.02.011. http://linkinghub.elsevier.com/retrieve/pii/S1751616114000435.

[14] Luo S, Xu C, Chen A, Zhang X. Experimental investigation of the response of gelatine behind the soft body armor. Forensic Sci Int 2016;266:8–13. http://dx.doi.org/10.1016/j.forsciint.2016.04.019. http://linkinghub.elsevier.com/retrieve/pii/S0379073816301712.

[15] Fackler ML, Malinowski JA. Ordnance gelatin for ballistic studies: detrimental effect of excess heat used in gelatin preparation. Am J Forensic Med Pathol 1988;9(3). http://journals.lww.com/amjforensicmedicine/Fulltext/1988/09000/Ordnance_Gelatin_for_Ballistic_Studies_.8.aspx.

[16] Cronin DS, Falzon C. Characterization of 10% ballistic gelatin to evaluate temperature, aging and strain rate effects. Exp Mech 2011;51(7):1197–206. http://dx.doi.org/10.1007/s11340-010-9438-z. http://link.springer.com/10.1007/s11340-010-9438-z.

[17] Mauzac O., Paquier C., Debord E., Jacquet J.F.. A substitute of gelatin for the measurement of dynamic back face deformation, Canada; 2010, https://www.researchgate.net/profile/Olivier_Mauzac/publication/236842973_A_substitute_of_gelatin_for_the_measurement_of_dynamic_back_face_deformation/links/00b7d5195438ed74cc000000.pdf.

[18] Mrozek RA, Leighliter B, Gold CS, Beringer IR, Yu JH, VanLandingham MR, et al. The relationship between mechanical properties and ballistic penetration depth in a viscoelastic gel. J Mech Behav Biomed Mater 2015;44:109–20. http://dx.doi.org/10.1016/j.jmbbm.2015.01.001. http://linkinghub.elsevier.com/retrieve/pii/S1751616115000028.

[19] Taddei L, Awoukeng Goumtcha A, Roth S. Smoothed particle hydrodynamics formulation for penetrating impacts on ballistic gelatine. Mech Res Commun 2015;70:94–101. http://dx.doi.org/10.1016/j.mechrescom.2015.09.010. http://linkinghub.elsevier.com/retrieve/pii/S0093641315001597.

[20] Wen Y, Xu C, Wang H, Chen A, Batra R. Impact of steel spheres on ballistic gelatin at moderate velocities. Int J Impact Eng 2013;62:142–51. http://dx.doi.org/10.1016/j.ijimpeng.2013.07.002. http://linkinghub.elsevier.com/retrieve/pii/S0734743X13001401.

[21] Wen Y, Xu C, Wang S, Batra R. Analysis of behind the armor ballistic trauma. J Mech Behav Biomed Mater 2015;45:11–21. http://dx.doi.org/10.1016/j.jmbbm.2015.01.010. http://linkinghub.elsevier.com/retrieve/pii/S1751616115000193.

[22] Bracq A, Haugou G, Delille R, Lauro F, Roth S, Mauzac O. Experimental study of the strain rate dependence of a synthetic gel for ballistic blunt trauma assessment. J Mech Behav Biomed Mater 2017;72:138–47. http://dx.doi.org/10.1016/j.jmbbm.2017.04.027. http://www.sciencedirect.com/science/article/pii/S175161611730187X.

[23] Kolsky H. An investigation of the mechanical properties of materials at very high rates of loading. Proc Phys Soc Sect B 1949;62(11):676–700. http://stacks.iop.org/0370-1301/62/i=11/a=302.

[24] Salisbury CP, Cronin DS. Mechanical properties of ballistic gelatin at high deformation rates. Exp Mech 2009;49(6):829–40. http://dx.doi.org/10.1007/s11340-008-9207-4. http://link.springer.com/10.1007/s11340-008-9207-4.

[25] Van Sligtenhorst C, Cronin DS, Wayne Brodland G. High strain rate compressive properties of bovine muscle tissue determined using a split Hopkinson bar apparatus. J Biomech 2006;39(10):1852–8. http://dx.doi.org/10.1016/j.jbiomech.2005.05.015. http://linkinghub.elsevier.com/retrieve/pii/S0021929005002332.

[26] Morin D, Haugou G, Bennani B, Lauro F. Experimental characterization of a toughened epoxy adhesive under a large range of strain rates. J Adhes Sci Technol 2011;25(13):1581–602. http://dx.doi.org/10.1163/016942410X524417. http://www.tandfonline.com/doi/abs/10.1163/016942410X524417.

[27] Morin D, Haugou G, Lauro F, Bennani B, Bourel B. Elasto-viscoplasticity behaviour of a structural adhesive under compression loadings at low, moderate and high strain rates. J Dyn Behav Mater 2015;1(2):124–35. http://dx.doi.org/10.1007/s40870-015-0010-x. http://link.springer.com/10.1007/s40870-015-0010-x.

[28] Lauro F, Bennani B, Croix P, Oudin J. Identification of the damage parameters for anisotropic materials by inverse technique: application to an aluminium. J Mater Process Technol 2001;118(1):472–7. http://www.sciencedirect.com/science/article/pii/S0924013601009906.

[29] Markiewicz E, Langrand B, Notta-Cuvier D. A review of characterisation and parameters identification of materials constitutive and damage models: from normalised direct approach to most advanced inverse problem resolution. Int J Impact Eng 2017. http://dx.doi.org/10.1016/j.ijimpeng.2017.01.028. http://www.sciencedirect.com/science/article/pii/S0734743X16307746.

[30] Fontenier B, Hault-Dubrulle A, Drazetic P, Fontaine C, Naceur H. On the mechanical characterization and modeling of polymer gel brain substitute under dynamic rotational loading. J Mech Behav Biomed Mater 2016;63:44–55. http://dx.doi.org/10.1016/j.jmbbm.2016.06.008. http://linkinghub.elsevier.com/retrieve/pii/S1751616116301746.

[31] Wu JZ, Dong RG, Schopper AW. Analysis of effects of friction on the deformation behavior of soft tissues in unconfined compression tests. J Biomech 2004;37(1):147–55. http://dx.doi.org/10.1016/S0021-9290(03)00240-9. http://linkinghub.elsevier.com/retrieve/pii/S0021929003002409.

[32] Oliveira I, Teixeira P, Ferreira F, Reis A. Inverse characterization of material constitutive parameters for dynamic applications. Procedia Eng 2015;114:784–91. http://dx.doi.org/10.1016/j.proeng.2015.08.027. http://www.sciencedirect.com/science/article/pii/S1877705815016665.

[33] Azar FS, Metaxas DN, Miller RT, Schall MD. Methods for predicting mechanical deformations in the breast during clinical breast biopsy. Bioengineering conference, 2000. Proceedings of the IEEE 26th annual Northeast. IEEE; 2000. p. 63–4. http://ieeexplore.ieee.org/abstract/document/842380/.

[34] Cronin DS. Ballistic gelatin characterization and constitutive modeling. In: Proulx T, editor. Dynamic behavior of materials, Volume 1: proceedings of the 2011 annual conference on experimental and applied mechanics. New York, NY: Springer New York; 2011. p. 51–5. ISBN 978-1-4614-0216-9

[35] Ravikumar N, Noble C, Cramphorn E, Taylor ZA. A constitutive model for ballistic gelatin at surgical strain rates. J Mech Behav Biomed Mater 2015;47:87–94. http://dx.doi.org/10.1016/j.jmbbm.2015.03.011. http://linkinghub.elsevier.com/retrieve/pii/S1751616115000922.

[36] Yang L, Shim V, Lim C. A visco-hyperelastic approach to modelling the constitutive behaviour of rubber. Int J Impact Eng 2000;24(6–7):545–60. http://dx.doi.org/10.1016/S0734-743X(99)00044-5. http://linkinghub.elsevier.com/retrieve/pii/S0734743X99000445.

[37] Du Bois P.. A simplified approach to the simulation of rubber-like materials under dynamic loading. 2003, p. 31–46.

[38] Zhao H, Gary G. A three dimensional analytical solution of the longitudinal wave propagation in an infinite linear viscoelastic cylindrical bar. application to experimental techniques. J Mech Phys Solids 1995;43(8):1335–48. http://dx.doi.org/10.1016/0022-5096(95)00030-M. http://www.sciencedirect.com/science/article/pii/002250969500030M.

[39] Gary G., Degreef V.. DAVID, Users' manual version, Labview version. LMS Polytechnique; Palaiseau, France; 2008. Version 12341.

[40] Rivlin RS. Large elastic deformations of isotropic materials. IV. Further developments of the general theory. Philos Trans R Soc A 1948;241(835):379–97. http://

dx.doi.org/10.1098/rsta.1948.0024. http://rsta.royalsocietypublishing.org/cgi/doi/10.1098/rsta.1948.0024.
A. Holzapfel GA. Nonlinear solid mechanics: a continuum approach for engineering. john wiley & sons Chichester: Wiley978-0-471-82319-3; 2000. OCLC: 838650783.
B. Liu I-S. A note on the Mooney–Rivlin material model. Continuum Mech Thermodyn 2012;24(4–6):583–90. http://dx.doi.org/10.1007/s00161-011-0197-6. http://link.springer.com/10.1007/s00161-011-0197-6.
C. Meng H, Li QM. Correlation between the accuracy of a SHPB test and the stress uniformity based on numerical experiments. Int J Impact Eng 2003;28(5):537–55. http://dx.doi.org/10.1016/S0734-743X(02)00073-8. http://www.sciencedirect.com/science/article/pii/S0734743X02000738.
[44] Lu Y, Zhang S. Study on interface friction model for engineering materials testing on split hopkinson pressure bar tests. Mod Mech Eng 2013;03(01):27–33. http://dx.doi.org/10.4236/mme.2013.31003. http://www.scirp.org/journal/PaperDownload.aspx?DOI=10.4236/mme.2013.31003.
[45] Roth S, Torres F, Feuerstein P, Thoral-Pierre K. Anthropometric dependence of the response of a thorax FE model under high speed loading: validation and real world accident replication. Comput Methods Programs Biomed 2013;110(2):160–70. http://dx.doi.org/10.1016/j.cmpb.2012.11.004. http://linkinghub.elsevier.com/retrieve/pii/S0169260712003021.